Brazilian Journal of Physics (2026) 56:4
https://doi.org/10.1007/s13538-025-01930-7

Plasma-Activated Water Generated by Surface-Wave Sustained Discharge: Physicochemical Properties and Antimicrobial Efficacy

M. Shiotani[1] · L. Gonçalves[1] · F. Miranda[2] · L. D. Leite[2] · V. K. F. Tavares[2] · N. F. Azevedo Neto[1] · C. Alves Junior[1,3] · C. Koga-Ito[2] · R. S. Pessoa[1]

Received: 13 August 2025 / Accepted: 16 October 2025

Abstract

Electrode-less surface-wave sustained discharge (SWD) plasma jets operated with noble gases provide a chemically clean and reproducible route to plasma-activated water (PAW) generation, avoiding electrode erosion and metal contamination while enabling long, stable activations. Using an argon SWD jet (70 W), we tracked the time-resolved thermal and physicochemical evolution of PAW over 40 min and assessed antimicrobial efficacy. PAW acidified to pH ~ 3.34, with ORP ~ 230 mV, conductivity ~ 180 µS/cm, and TDS ~ 55 mg L^{-1}. Spectrophotometric/colorimetric analyses showed the accumulation of RONS with H_2O_2 ~ 10–25 mg L^{-1}, NO_3^- ~ 10–25 mg L^{-1}, and $NO_2^- \leq 1$ mg L^{-1}; evaporation during long activations concentrated solutes, and volume-normalized endpoints confirmed that qualitative trends persist after correcting for mass loss. Optical emission and thermal probes indicated that water buffers the heat load yet can drift toward ~ 40 °C under the longest activations, motivating temperature control (≤ 20–25 °C) to preserve thermally labile ROS. Microbiological assays revealed strong bactericidal activity against *Staphylococcus aureus* and *Escherichia coli* but limited effect on *Candida albicans*, consistent with organism-specific cell-wall structure and oxidative defenses. The batch energy input (46.67 Wh for 40 mL) corresponds to EPL ≈ 1.17 kWh L^{-1}, highlighting a purity–energy trade-off relative to some DBD systems; we outline straightforward optimizations (minor O_2/N_2 admixtures, reduced gap, bubbling/recirculation, and active cooling) to enhance RONS yield and energy efficiency without compromising chemical purity. Collectively, these results establish electrode-less SWD as a robust platform for sterile, contamination-free PAW and clarify operational levers that tune performance for biomedical and sanitation applications.

Keywords Plasma-activated water · Cold atmospheric plasma · Reactive oxygen and nitrogen species · Antimicrobial efficacy · Surface-wave sustained discharge

1 Introduction

Cold Atmospheric Plasmas (CAPs) have attracted widespread interest for their capacity to generate plasma-activated liquids (PALs), especially plasma-activated water (PAW), which has a diverse range of applications in biomedicine, agriculture, and disinfection [1–5]. The efficacy of PAW derives largely from its high concentration of reactive oxygen and nitrogen species (RONS), including nitrates, nitrites, and hydrogen peroxide, formed during interactions between plasma and water [6, 7]. These reactive species grant PAW its distinctive physicochemical properties, enabling potent activity against various microorganisms [6–8].

The design and operational parameters of the plasma generator are critical determinants of both the characteristics of the plasma produced and the subsequent properties of PAW.

✉ M. Shiotani
marcondes.micaela5@gmail.com

✉ R. S. Pessoa
rspessoa@ita.br

[1] Plasmas and Processes Laboratory (LPP), Aeronautics Institute of Technology (ITA), São José Dos Campos, SP, Brazil

[2] Department of Environment Engineering, Institute of Science and Technology, São Paulo State University (UNESP), São José Dos Campos, SP, Brazil

[3] Universidade Federal Rural Do Semiárido (UFERSA), Mossoró, RN, Brazil

Published online: 27 October 2025

Multiple plasma generation methods, such as dielectric barrier discharge (DBD), gliding arc, and surface-wave sustained discharge (SWD), have been explored to address different practical needs. DBD plasma generators, for instance, produce non-thermal plasma at atmospheric pressure and effectively synthesize RONS in water but can be limited by plasma stability and uniform RONS distribution [9]. Gliding arc systems operate with increased energy efficiency and generate significant quantities of RONS to enhance the antimicrobial properties of PAW. These systems function at higher temperatures, which requires appropriate thermal management [10, 11].

More recently, surface-wave sustained discharge (SWD) systems have emerged as an advanced alternative. By operating at microwave frequencies, often with noble gases such as argon, and avoiding the use of electrodes, SWD systems minimize electrode degradation and eliminate the risk of metal contamination in the treated liquid. Unlike many low-power AC-driven plasma sources where the working gas is in direct contact with electrodes, the SWD configuration couples microwave energy through a dielectric tube (e.g., quartz), sustaining the plasma remotely and ensuring a high-purity plasma–liquid interaction environment. This electrode-less design enhances the reproducibility and reliability of PAW, which is particularly valuable for applications requiring high chemical purity, such as biomedical disinfection, food safety, and surface processing [12, 13]. Furthermore, SWD systems produce high-density, spatially uniform plasma columns with relatively high electron densities even at atmospheric pressure, enabling more stable and consistent RONS generation during extended activation periods.

Despite considerable advancements, research gaps persist concerning how plasma parameters influence PAW's antimicrobial capabilities against diverse microbial targets. Important factors such as activation time, gas composition, and the specific plasma system significantly impact RONS concentration, which in turn drives antimicrobial efficacy [14, 15]. The mechanisms through which various microorganisms, including fungi like *Candida albicans*, respond to PAW are not yet fully clarified, as some organisms display resistance under particular conditions [1–4].

Addressing these uncertainties is essential to refine PAW-based technologies for targeted disinfection and sterilization. Moreover, PAW has garnered attention in multiple sectors owing to its eco-friendly profile. In healthcare, its non-toxic nature presents a promising route for combating antibiotic-resistant pathogens [3, 16]. In agriculture, the potential to enhance crop protection while reducing chemical inputs highlights PAW's role in sustainable farming. Optimizing plasma parameters in PAW can generate tailored RONS for targeted uses [17]. Adjusting plasma conditions allows for customized PAW solutions in disinfection, sterilization, and therapeutic applications across industries.

Progress in CAP research has proceeded from fundamental plasma–liquid interactions to more detailed investigations of the biochemical pathways responsible for microbial inactivation [18]. PAW, which contains RONS, can affect membranes, proteins, and DNA, leading to the elimination of bacteria, viruses, and fungi [19]. Several studies have confirmed the antimicrobial activity of PAW [20–22]. For example, one investigation using a coaxial DBD reactor demonstrated that PAW generated with compressed air, helium, or argon could achieve a 99.99% reduction of *Staphylococcus aureus* and *Escherichia coli* after just 10 min. However, *Candida albicans* proved more resilient, displaying a reduction rate between 12.05% and 39.76% depending on the gas used, which increased to 53.41% for argon-based PAW after 30 min [23]. Another study highlighted PAW's capacity to significantly decrease *Pseudomonas aeruginosa* biofilm viability, emphasizing the need to optimize RONS composition to maximize efficacy against a wide range of pathogens [20]. In food safety applications, PAW treatment effectively inactivated *Salmonella enterica* and *Listeria monocytogenes* on fresh produce, reducing microbial loads by up to 5 log units, underscoring its promise as a safe, non-toxic substitute for conventional disinfectants [24]. Collectively, these findings demonstrate the versatility of PAW while also highlighting the variability inherent in its performance due to differences in microorganism type and plasma generation techniques [25]. Optimizing factors such as the choice of gas, treatment duration, and plasma parameters can markedly enhance the antimicrobial efficacy of PAW. Advances in plasma technology, particularly with the development of SWD systems, have broadened the scope of applications by providing stable, controllable plasma conditions that may be customized for specific microbial challenges.

In this context, electrode-less SWD plasma jets operated with noble gases provide a method for PAW generation that reduces electrode erosion and metal contamination, while allowing for extended and consistent activations. This study therefore asks: (i) how does SWD activation time modulate the coupled thermal and physicochemical evolution of PAW (pH, ORP, σ, TDS, DO, and time-resolved RONS)? (ii) can an SWD argon jet produce bactericidal PAW without direct bubbling or electrode contact while preserving chemical purity? and (iii) which operational factors (thermal budget, evaporation, gas–liquid coupling) explain organism-dependent efficacy, particularly the contrast between bacteria and *Candida albicans*? Addressing these questions clarifies the trade-offs between purity, energy per liter, and antimicrobial performance and guides targeted optimization for biomedical and sanitation uses.

2 Experimental

2.1 SWD Plasma Jet Configuration and Diagnostic Procedures

As shown in Fig. 1, the experimental setup consists of a Surface-Wave Sustained Discharge (SWD) system operating at a frequency of 2.45 GHz, powered by a solid-state power supply (Sairem, GMS 200, France) with a maximum capacity of 200 W.

Within the SWD cavity, a quartz tube (inner diameter 4 mm, outer diameter 6 mm) channels a steady flow of argon gas (99.95% purity), regulated by a rotameter. The reactor tip is positioned 17 mm above the DI water surface. Throughout the activation process, the system is continuously cooled with compressed air to prevent thermal degradation and maintain the structural integrity of the quartz tube. In practice, 70 W ensured robust surface-wave propagation and column stability, and a 2.5 L min^{-1} argon flow produced a steady, laminar impingement at the 17 mm nozzle–liquid spacing, minimizing turbulence and splashing that would otherwise confound thermal and mass-loss measurements.

2.2 Optical Characterization of the SWD Plasma

To characterize the plasma produced by the SWD system, Optical Emission Spectroscopy (OES) was employed across a broad spectral range of 200–1100 nm. Emission spectra were recorded using an OceanHDX spectrometer, enabling the detection and identification of atomic, ionic, and molecular species within the discharge. An optical fiber, equipped with a collection lens, was positioned approximately 5 cm in front the of the plasma jet to optimize signal acquisition and ensure a representative spectral capture. To balance temporal resolution with analysis sensitivity, two distinct integration times (20 ms and 1000 ms) were used, facilitating the detection of both intense and less prominent emissions.

2.3 Production of PAW

For each experimental run, 40 mL of deionized (DI) water (Gehaka OS10MAX) was dispensed into a Petri dish (95 mm diameter, 15 mm height) serving as the substrate for plasma activation. The SWD argon jet was directed toward the water surface to ensure direct jet–liquid interaction. All experiments were performed under uniform conditions: constant applied power of 70 W and argon carrier gas at 2.5 L min^{-1} (slm), with plasma exposure of up to 40 min to enable reliable, cross-sample comparisons. The operating point (70 W, 2.5 L min^{-1} Ar, 17 mm nozzle–liquid gap) was selected to sustain a stable, self-sustained SWD column and reproducible plasma–liquid coupling without overheating the quartz (with forced-air cooling), while maintaining a laminar, splash-free jet that preserves mass-loss tracking, optical alignment, and controlled gas–liquid transfer. Because prolonged activation warms the liquid and H_2O_2 is thermally labile at acidic pH, we recommend maintaining the PAW bath at $\leq$ 20–25 °C during activation using a jacketed beaker (recirculating chiller) or an ice-bath support. Immediately after activation, samples should be cooled to room temperature and stored cold to minimize ROS decomposition. Although our setup already included forced-air cooling of the discharge tube, these practices clarify best-in-class thermal management for the liquid phase.

2.4 Characterization of PAW

2.4.1 Analysis of Physicochemical Parameters

A comprehensive evaluation of key physicochemical parameters was performed on the plasma-activated liquids, including pH, electrical conductivity (σ), total dissolved solids (TDS), and oxidation–reduction potential (ORP). These parameters were monitored dynamically in real time using a Metrohm 913 pH meter, ensuring high accuracy and capturing transient changes during plasma activation. Dissolved oxygen (DO) levels were determined with an AK87 V2 (AKSO) meter, which was also used at regular intervals to assess variations over the course of the experiment. In addition, the mass loss of each sample was monitored in real-time with a Marte precision semi-analytical balance (Fig. 2). Collectively, these data provide critical insight into the plasma-induced modifications occurring in the treated liquids.

2.4.2 Thermal Analysis of Plasma-Liquid Interaction

A Hukseflux FHF03-02 heat flux sensor, coupled to a Hioki LR8432-20 data logger operating at 10 ms resolution, was employed to measure temperature and thermal flux over a 40 min interval, starting from plasma ignition. As illustrated in Fig. 3, the sensor's probe was positioned at the bottom of the Petri dish under two conditions: (1) With 40 mL DI water, where the plasma jet was 17 mm above the water surface; (2) Without liquid, maintaining a 27 mm gap between the plasma nozzle and the dish bottom. This setup enabled a direct comparison of heat transfer dynamics in the presence and absence of water.

2.4.3 Analysis of RONS

To monitor plasma-induced chemical changes in real time, we recorded ultraviolet–visible (UV–Vis) spectra (Thermo Scientific Evolution 220) over 190–270 nm, enabling qualitative identification of reactive oxygen and nitrogen

(a)

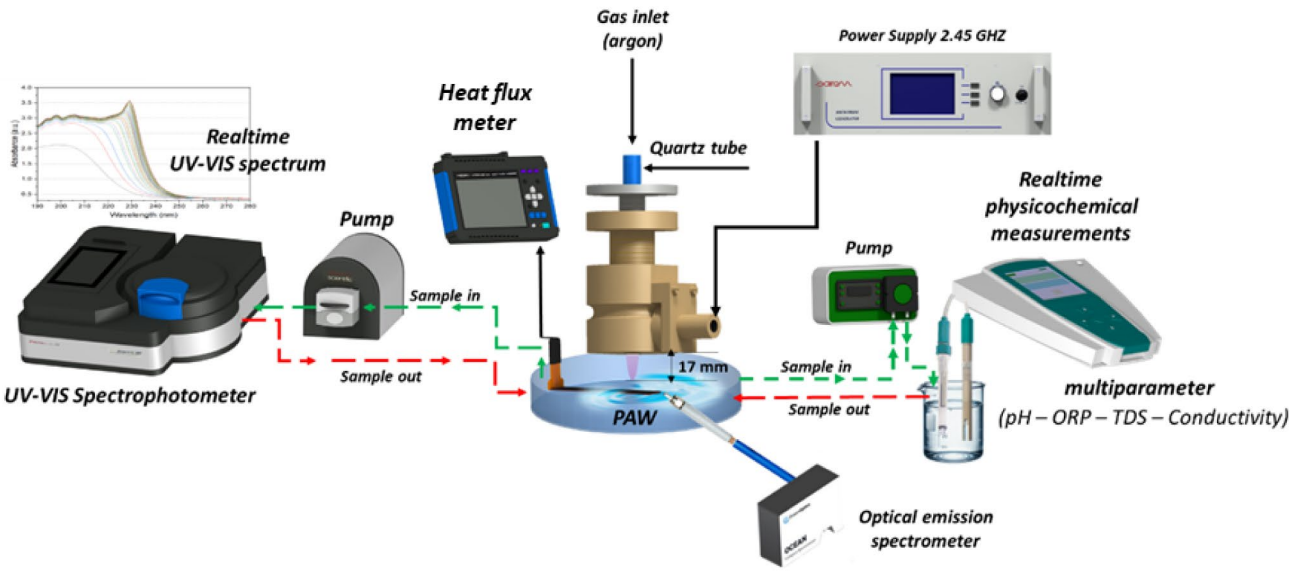

(b)

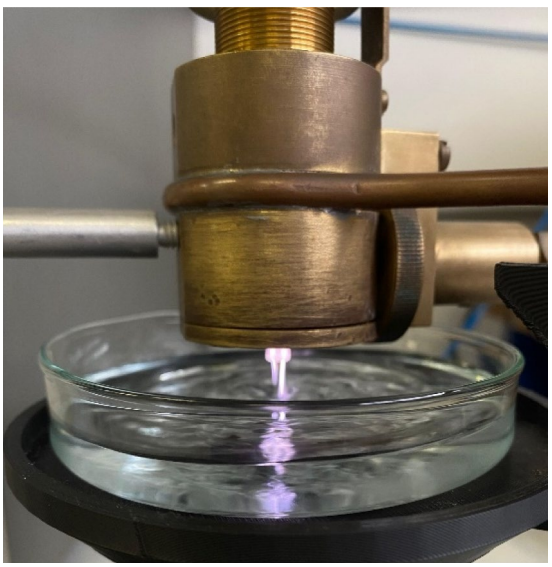

Fig. 1 **a** Schematic of the Surface Wave Sustained Discharge (SWD) system used for Plasma-Activated Water (PAW) generation, illustrating the 2.45 GHz power supply, quartz tube for argon gas input, heat flux meter, and in-line analytical devices for real-time measurements: optical emission spectroscopy (OES), UV–Vis spectrophotometry, and a multiparameter meter providing dynamic pH, ORP, TDS, and electrical conductivity data. **b** Photo illustrating the SWD system and the generated argon plasma jet interacting with the DI water. Typical operating point during PAW activation: 70 W, 2.5 L min^{-1} Ar, 17 mm nozzle–liquid gap

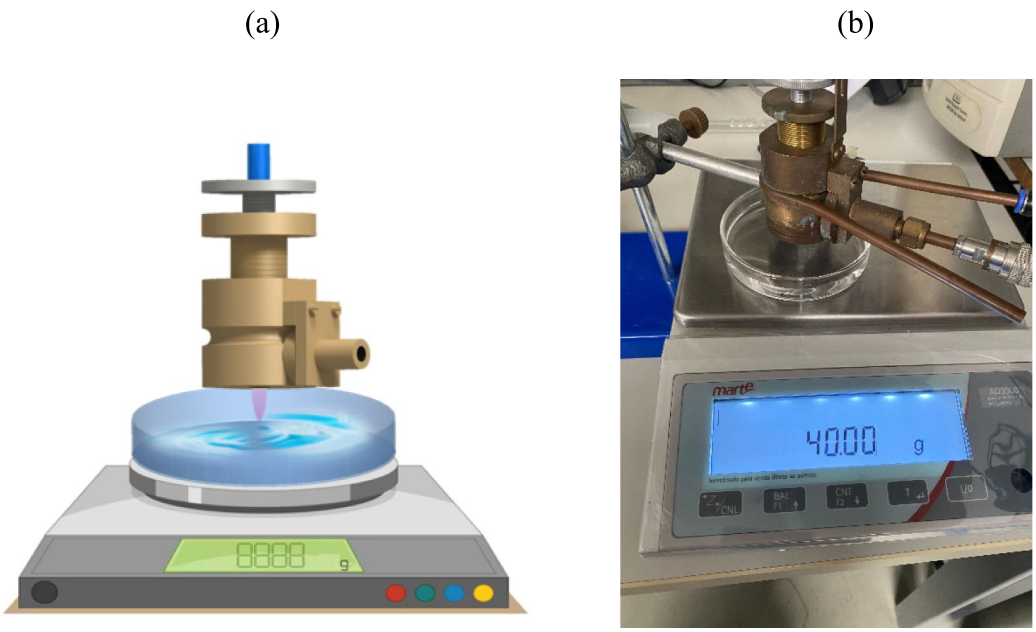

Fig. 2 (**a**) Schematic illustration of real-time mass loss monitoring during plasma activation of the liquid; (**b**) Photograph depicting the experimental setup

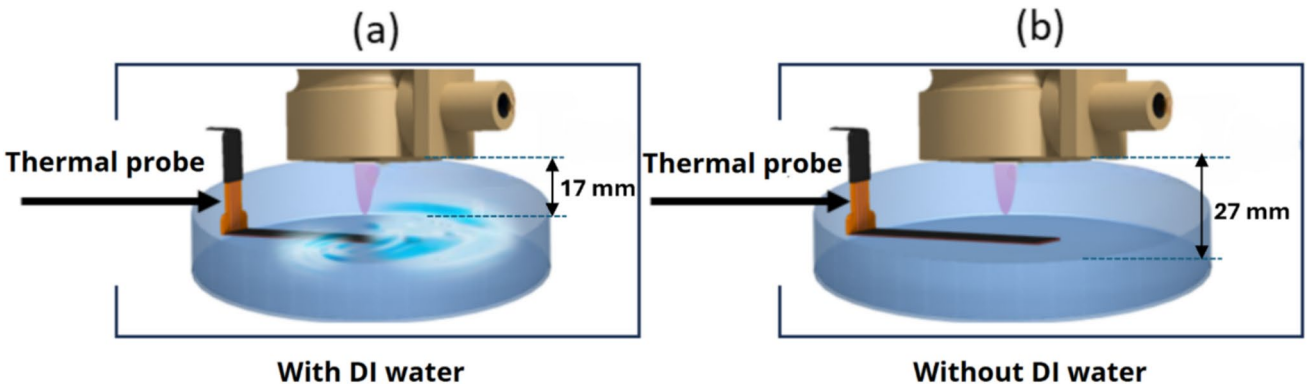

Fig. 3 Schematic representations of the experimental setup, highlighting the thermal probe placement at the bottom of the Petri dish: (**a**) with 40 mL DI water (plasma nozzle 17 mm above the water surface), and (**b**) without liquid (27 mm between the plasma nozzle and the dish bottom)

species (RONS) via characteristic absorption features. Complementarily, quantitative concentrations of nitrate (NO_3^-), nitrite (NO_2^-), and hydrogen peroxide (H_2O_2) were obtained with a Micro 20 Multiparameter Photometer (AKSO) using device-specific test strips: NO_3^- (0–60.0 ppm), NO_2^- (0.01–1.80 ppm), and H_2O_2 (0.3–100 ppm). Measurements were taken at 0, 2.5, 5, 10, 15, 20, 25, 30, 35, and 40 min, allowing a time-resolved assessment of RONS evolution during activation. We note that colorimetric strips exhibit finite low-end sensitivity and potential cross-interference—particularly a downward bias in NO_2^- readings in oxidant-rich matrices (e.g., in the presence of H_2O_2); therefore, sub-ppm NO_2^- values should be interpreted with appropriate caution.

2.5 Microbiological Assays

Following the methodologies employed by Chiappim et al. [26], we utilized reference microbial strains, including the Gram-positive bacterium *S. aureus* (ATCC 6538), the Gram-negative bacterium *E. coli* (ATCC 10799), and the fungus *C. albicans* (SC 5314). The detailed procedure of the tests and microbiological analysis is represented in the flowchart in Fig. 4**.**

Bacterial cultures were propagated in Heart Infusion Broth (BHI), and the fungal strain was cultured on Sabouraud Dextrose Agar. The cultures were incubated aerobically at 37 °C for 24 h.

Standardized microbial suspensions with a concentration of 10^6 cells/mL were prepared in sterile saline solution (0.9%

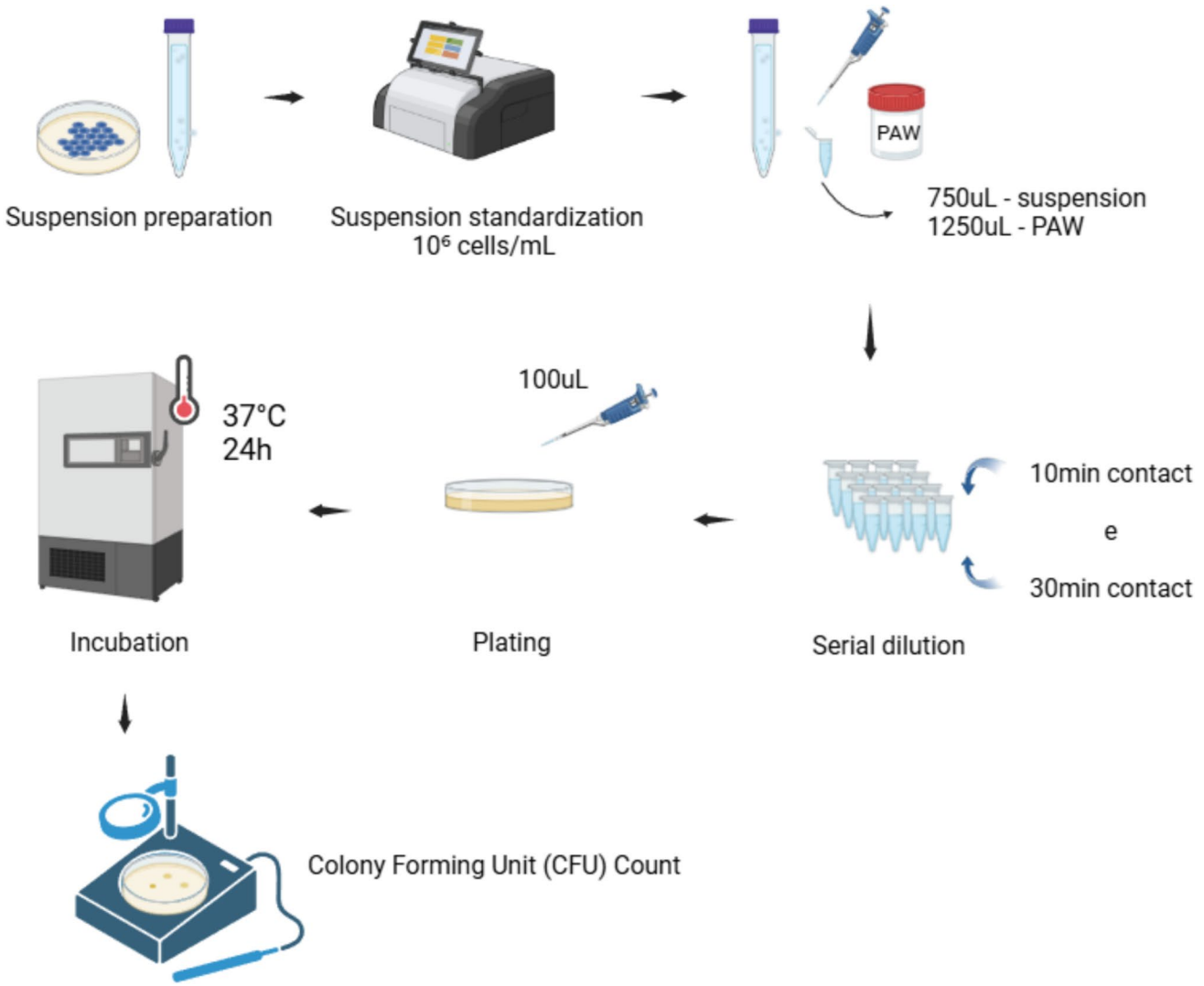

Fig. 4 Workflow of microbiological assays, including suspension preparation, treatment with PAW, serial dilution, plating, incubation, and colony-forming unit (CFU) counting

NaCl), using a spectrophotometer (AJX-1600, Micronal, São Paulo, SP, Brazil) to ensure uniformity. Spectrophotometric measurements were conducted at $\lambda = 490$ nm with an optical density (O.D.) of 0.374 for *S. aureus*, $\lambda = 600$ nm with an O.D. of 0.050 for *E. coli*, and $\lambda = 530$ nm with an O.D. of 0.138 for *C. albicans*.

The antimicrobial activity was assessed using the following test groups: deionized water (control), PAW activated for 10 min, and for 40 min. The 40-min activation time was not extended further due to the considerations mentioned previously, such as increased temperature, sample loss, and the need to retain sufficient volume for analyses. Glassware and saline were sterilized (autoclave); freshly generated PAW was used without sterilization under aseptic handling. A mixture of 750 µL of the microbial suspension and 1250 µL of PAW was combined in microtubes, homogenized, and incubated for periods of 10 and 30 min. Serial dilutions were subsequently prepared in sterile saline. An aliquot of 100 µL from each dilution was spread onto Brain Heart Infusion Agar for the Gram-positive bacterium *S. aureus* and the Gram-negative bacterium *E. coli*, and onto Sabouraud Dextrose Agar for *C. albicans*, using the spread plate technique described by Miles et al. [27]. After incubation at 37 °C for 24 h under aerobic conditions, colonies were counted and colony-forming units per milliliter (CFU/mL) were calculated. Each condition was tested in triplicate across three independent experiments (total $n = 9$ per group). Data are reported as mean ± SD. Statistical analyses and graphing were performed in GraphPad Prism v7.0 (GraphPad Software, San Diego, CA, USA). Group differences were evaluated by one-way ANOVA followed by Tukey's post hoc test for pairwise comparisons (two-tailed, $\alpha = 0.05$).

3 Results and Discussion

3.1 Spectroscopic Characterization of the SWD Plasma Jet–Liquid Interaction

Optical emission spectroscopy (OES) was employed to probe the species generated by the SWD argon plasma, both in free-jet mode (no contact with DI water) and with the plasma directly impinging on the liquid. Figures 5(a) and 5(c) show the emission spectra over a broad wavelength range (200–1100 nm), while Figs. 5(b)and 5(d) present a magnified view of the 200–700 nm region. Analyzing these spectra provides insight into the active plasma species and their contributions to the plasma chemistry, particularly in forming RONS that underpin PAW activity.

In the full-range spectrum [Fig. 5(a)], several prominent peaks in the visible and near-infrared region correspond to atomic argon (Ar I) transitions at approximately 696.5 nm, 706.7 nm, 727.2 nm, 738.4 nm, 751.5 nm, 763.5 nm, 772.4 nm, 794.8 nm, 800.6 nm, 811.5 nm, 842.5 nm, and 912.3 nm [28, 29]. Argon emissions dominate since it is the working gas; their intensity indicates the plasma's energy distribution and argon excitation, both crucial in producing reactive species at the liquid interface.

Zooming into the 200–700 nm range [Fig. 5(b)] reveals additional bands that arise from nitrogen- and oxygen-containing species. A strong peak at 337.1 nm corresponds to the second positive system of molecular nitrogen (N_2), specifically the $C^3\Pi_u \rightarrow B^3\Pi_g$ transition. Another N_2-related peak is observed near 357.7 nm, further indicating the presence

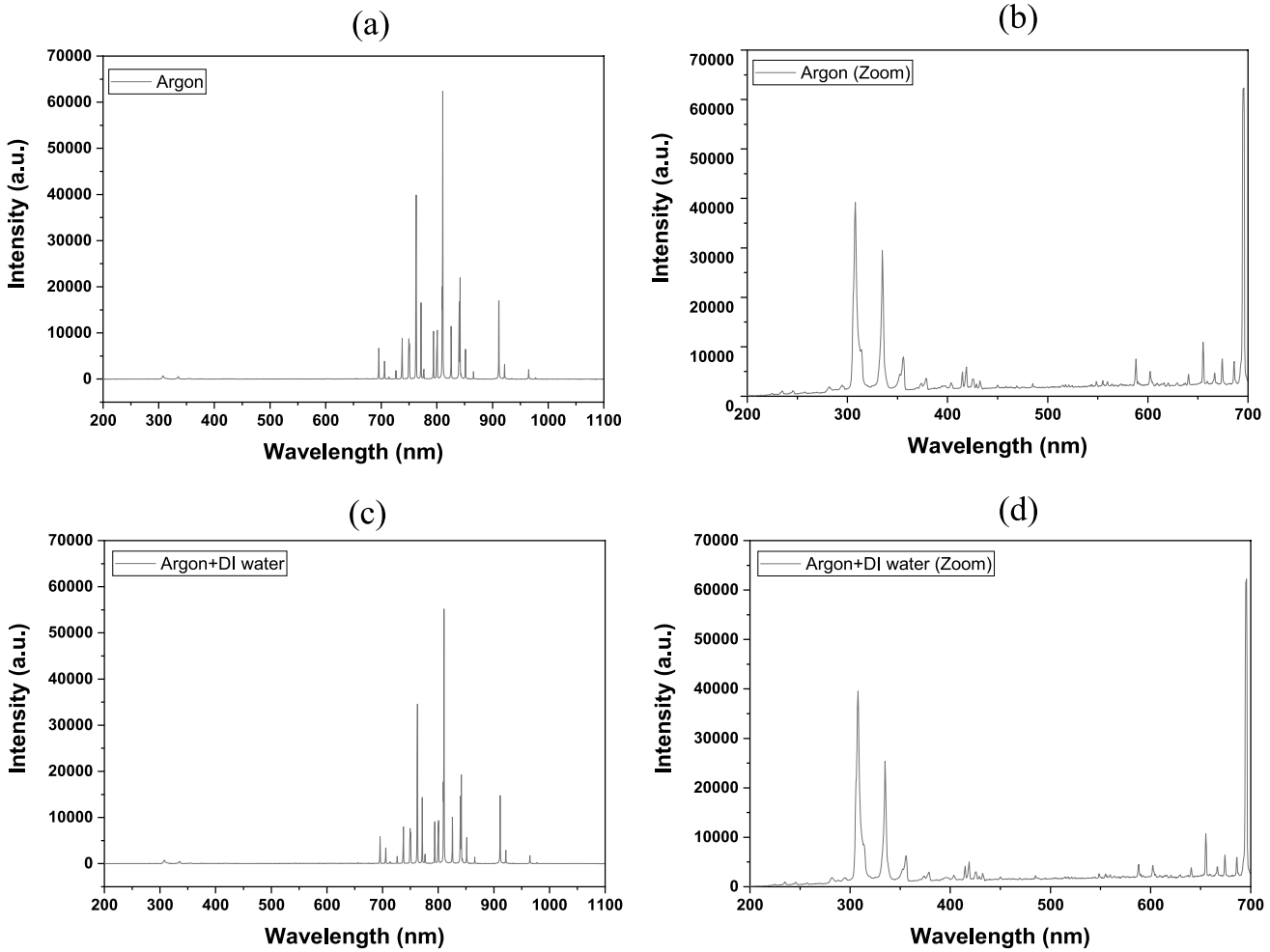

Fig. 5 Optical emission spectra of the electrode-less SWD argon jet (Ar flow 2.5 L min^{-1}; discharge power 70 W) acquired with the same collection geometry. (**a**) Dry Ar jet, full spectrum (200–1100 nm; integration time 20 ms). (**b**) Dry Ar jet, zoomed view of 200–700 nm acquired with longer integration (1000 ms) to resolve weak UV/visible features. (**c**) Ar jet impinging on deionized water, full spectrum (200–1100 nm; 20 ms). (**d**) Ar + DI water, zoomed 200–700 nm (1000 ms). Panels (b) and (d) use longer integration; therefore, intensities are not directly comparable to (a) and (c)

of excited molecular nitrogen. These emissions are relevant to the formation of nitrogen-based reactive species (e.g., NO_3^- and NO_2^-) essential for PAW chemistry.

Notably, an emission at 309 nm is assigned to the hydroxyl radical OH ($A^2\Sigma^+ \rightarrow X^2\Pi$), a highly reactive species central to plasma–liquid chemical pathways. This signal reflects interaction with water vapor or ambient moisture, underscoring the plasma's capacity to produce reactive oxygen species (ROS) involved in oxidation processes and microbial inactivation. Additionally, nitric oxide (NO) γ-bands between 250 and 280 nm point to nitrogen and oxygen interactions that yield reactive nitrogen species—another cornerstone of PAW's acidification and oxidative capabilities.

When argon plasma directly interacts with deionized water, the emission profile changes relative to the free-jet condition, as shown in Figs. 5(c) and 5(d). In the full-range spectrum [Fig. 5(c)], the intensities of the argon lines are generally reduced compared to the dry plasma case [Fig. 5(a)], reflecting energy losses through plasma–liquid interactions. Additionally, the presence of water vapor and water-surface reactions promotes the formation of OH and other oxygenated species, which can quench or redistribute energy among different emission channels.

A closer look at the 200–700 nm region [Fig. 5(d)] also reveals signals corresponding to OH (around 309 nm) and nitrogen-related transitions (e.g., N_2 and NO bands). These emissions are indicative of reactive oxygen and nitrogen species generated at or near the liquid interface. In particular, the stronger OH emission and the appearance of NO γ-bands highlight enhanced plasma–water chemistry, leading to the formation of RONS. This shift in emission profile confirms that liquid contact significantly alters the plasma's reactive environment.

While the OES analysis presented here is qualitative, we note its quantitative potential and the way it will be leveraged in follow-on work. In particular, rotational temperature can be retrieved from band-shape fitting of the N_2(C–B) second-positive system, vibrational temperature from appropriate N_2 band intensity ratios, and relative excited-species densities via actinometry with a calibrated spectral response (e.g., using Ar/N_2 as actinometers). Where signal-to-noise permits, OH(A–X) rotational thermometry may further constrain near-interface gas temperatures. Incorporating these diagnostics will enable direct correlation between plasma state (temperatures/species) and the time-resolved RONS yields reported here.

3.2 Thermal Analysis of Plasma-Liquid Interaction

The thermal behavior of an SWD argon plasma jet was investigated under two distinct conditions: (i) plasma activation without liquid and (ii) plasma activation in the presence of 40 mL of DI water. The results, presented in Fig. 6, elucidate both the magnitude and dynamics of heat transfer within the system.

In the absence of liquid, the heat flux [Fig. 6(a)] initially exhibits large negative values, indicating that the hotter plasma rapidly transfers heat to the comparatively

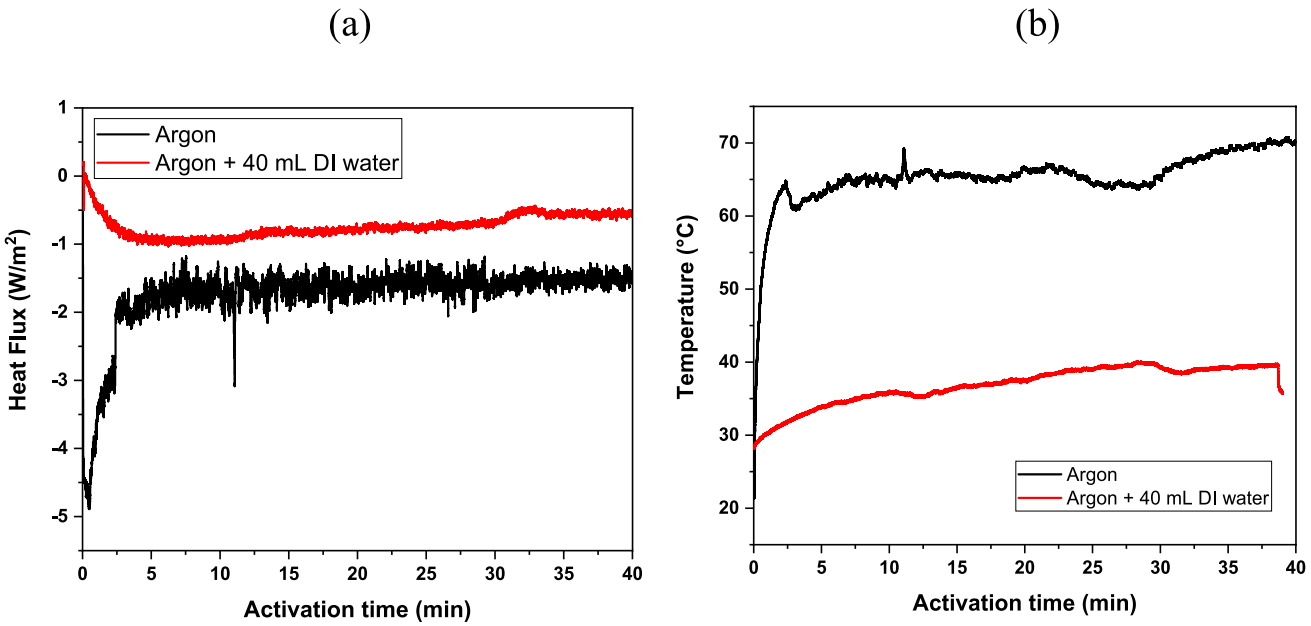

Fig. 6 Time traces of (**a**) heat flux and (**b**) temperature during electrode-less SWD-Ar operation with a 40 mL deionized-water load (red) versus dry operation without liquid (black). The presence of liquid markedly moderates heating: the heat-flux magnitude is reduced and the temperature stabilizes near ~ 38–40 °C, whereas dry operation reaches ~ 65–70 °C. Conditions were identical except for the liquid load (same power, gas, and geometry)

cooler sensor. This steep gradient stems from the significant temperature difference at plasma ignition, in accordance with the Zeroth Law of Thermodynamics. As time progresses, the magnitude of this negative heat flux diminishes, signaling a gradual movement toward thermal equilibrium. However, without the moderating influence of liquid, temperatures [Fig. 6(b)] escalate quickly, reflecting inefficient heat dissipation and abrupt thermal spikes.

By contrast, when DI water is introduced, two key effects are observed. First, the heat flux transitions more gently, with less pronounced negative values. Although a similar initial gradient exists, the liquid continuously absorbs and redistributes thermal energy, preventing large swings in temperature. Consequently, the water-containing system approaches a much lower equilibrium temperature—approximately 30 °C below that of the dry condition. Second, Fig. 6(b) reveals that the DI water temperature increases in a comparatively linear and stable manner, confirming the role of water as a thermal sink. The presence of water not only provides a reservoir for absorbing heat but also promotes convective currents, further aiding in uniform heat distribution.

From a plasma-chemistry standpoint, this moderated temperature rise has important implications. The absorbed thermal energy contributes to the partial dissociation of water molecules, fostering the production of reactive oxygen species (ROS) such as hydroxyl radicals (•OH) and hydrogen peroxide (H_2O_2). These species are fundamental drivers of oxidation and disinfection processes in PAW. Thus, the DI water bath not only protects the plasma–liquid interface from excessive heating, which could degrade or alter sensitive components, but also enhances the formation of critical ROS. Nonetheless, under the longest activation times the bulk liquid temperature was observed to drift toward ~ 40 °C, a condition that can accelerate the decomposition of thermally labile species such as H_2O_2 under acidic conditions. For this reason, maintaining the water at ≤ 20–25 °C during activation, using a jacketed beaker, ice-bath support, or recirculating chiller, and promptly cooling the samples afterward is recommended to preserve ROS stability. While this operational adjustment does not change the core findings of the study, it increases robustness and repeatability for downstream antimicrobial applications.

Ultimately, the marked difference in thermal behavior between the two scenarios underscores the dual function of DI water in plasma processes: it moderates temperature, thus improving process stability, and it supports key chemical reactions that underpin PAW's efficacy in diverse applications.

3.3 Analysis of Physicochemical Parameters

pH is a measure that expresses the concentration of hydrogen ions (H^+) in a solution, indicating its acidity or basicity. For water, pH typically ranges between 6.5 and 8.5, depending on factors such as the presence of impurities and the concentration of dissolved carbon dioxide [30]. However, when water is exposed to plasma, complex interactions between reactive chemical species, such as free radicals, ions, and RONS, lead to acidification due to the formation of acidic compounds. As a result, the pH of PAW tends to decrease significantly, especially with increased exposure time [31].

During the plasma activation of DI water by SWD argon plasma, a sharp drop in pH is observed in the initial moments (up to approximately 4 min), indicating significant acidification of the medium, as shown in Fig. 7a. This initial behavior is attributed to the rapid introduction of RONS into the aqueous medium, including nitric acid (HNO_3), hydroxyl radicals (OH), and hydrogen peroxide (H_2O_2), which trigger a series of chemical reactions and contribute to the formation of acidic compounds.

After the initial activation period, a more gradual decrease in pH is observed between 4 and 17 min, reflecting the continuation of chemical reactions at a more controlled rate. This suggests that the system begins to approach a dynamic equilibrium state. Between 17 and 38 min, the pH decreases linearly at a rate of approximately −0.00030 pH/s, reaching a value of around 3.34 at the end of the period. This pattern indicates that the system is still transitioning, but with more stabilized changes, suggesting a balance between the generation, dissolution, and saturation of reactive species.

The analysis of the curve shows that the impact of plasma is most pronounced in the early stages of activation, with the rapid and massive introduction of RONS leading to significant acidification of the medium. As the system progresses, the gradual stabilization of pH reflects the role of chemical saturation in regulating the system's conditions. These processes reinforce the relevance of pH as a key parameter for monitoring the chemical reactivity of plasma-activated solutions and their potential applications in various contexts [18].

The ability of a solution to oxidize or reduce another substance is evaluated by the oxidation–reduction potential (ORP), which is directly influenced by the concentration and strength of present oxidants. In Fig. 7b, a significant increase in ORP is observed in the first 4 min, reaching values close to 200 mV, followed by a more gradual increase until approximately 230 mV at the end of the activation period (38 min). This behavior reflects the rapid initial generation of RONS, such as peroxides, nitrates, and free radicals, which contribute to a highly oxidative environment.

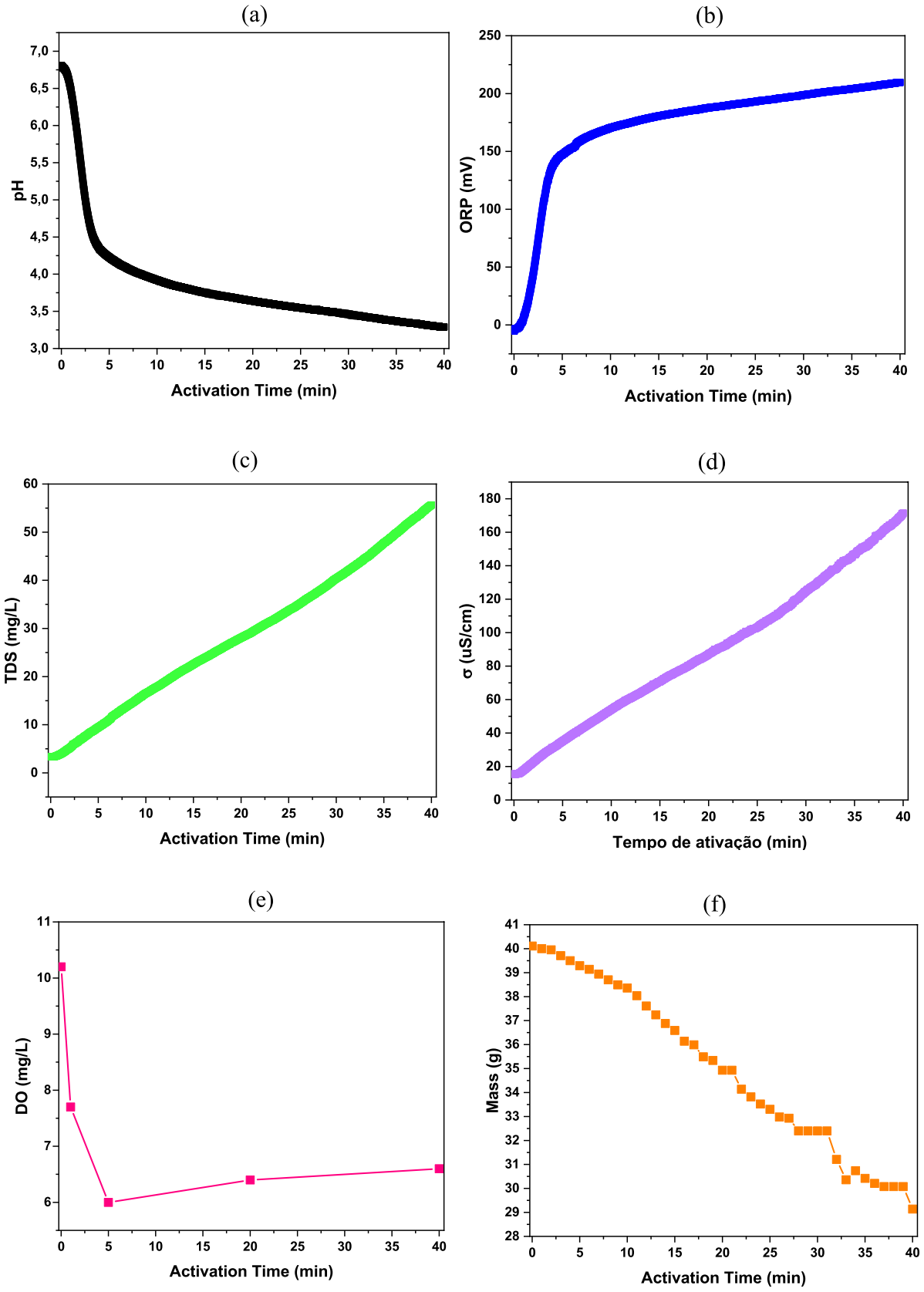
(a)
pH
Activation Time (min)
(b)
ORP (mV)
Activation Time (min)
(c)
TDS (mg/L)
Activation Time (min)
(d)
σ (uS/cm)
Tempo de ativação (min)
(e)
DO (mg/L)
Activation Time (min)
(f)
Mass (g)
Activation Time (min)

◂**Fig. 7** Time evolution of physicochemical parameters of deionized water during electrode-less SWD-Ar activation (0–40 min): (**a**) pH; (**b**) oxidation–reduction potential (ORP); (**c**) total dissolved solids (TDS); (**d**) electrical conductivity (σ); (**e**) dissolved oxygen (DO); and (**f**) sample mass recorded in real time. The trends show acidification with increasing oxidizing character (ORP), concomitant increases in TDS and conductivity, an initial DO drop followed by partial recovery, and progressive mass loss due to evaporation. These mass changes were later used to normalize concentration data

ORP is a particularly relevant parameter for disinfection applications, as it is directly related to the antimicrobial capacity of the activated solution. High ORP values are associated with the destruction of vital microbial components, such as lipids, proteins, and nucleic acids, leading to loss of cell viability [14, 31]. This process occurs due to structural damage to cell membranes and interference with microbial defense mechanisms. The behavior of ORP is inversely proportional to pH, as evidenced by the comparison between the pH and ORP curves. As pH decreases, the concentration of hydrogen ions increases, favoring more oxidative conditions. Conversely, as pH increases, the availability of oxidant species decreases, reducing the solution's oxidative potential. Thus, lower pH values and high ORP values create ideal conditions for antimicrobial action, highlighting the crucial role of this parameter in evaluating the chemical reactivity and effectiveness of plasma-activated solutions.

Total dissolved solids (TDS) refer to the concentration of dissolved substances in a solution, including ions, salts, minerals, and organic compounds. In the context of plasma activation, TDS is an important metric for monitoring chemical changes in the system, as it reflects the presence of new reactive species generated during the process. In Fig. 7c, a steady and linear increase in TDS is observed over the activation time, starting from values close to zero and reaching approximately 55 mg/L after 38 min. This increase is attributed to the dissolution of compounds formed through plasma-liquid interaction, such as nitrates, nitrites, and peroxides. As these compounds dissolve in the solution, they increase the concentration of charged particles, also influencing electrical conductivity. The linear behavior of TDS indicates that the generation of reactive species and their dissolution in the aqueous medium occur continuously and stably throughout the activation period.

Electrical conductivity (σ) measures a solution's ability to conduct electric current and is directly influenced by the concentration of dissolved ions, such as cations and anions. In the case of water, σ reflects the presence of salts, minerals, and other charged species that determine its conductivity. During plasma treatment, the rapid dissolution of reactive species such as nitrates, nitrites, and peroxides increases the density of free charges in the solution, leading to a continuous rise in electrical conductivity. In Fig. 7d, a linear increase in conductivity is observed over the activation time, starting at approximately 20 µS/cm and reaching around 180 µS/cm after 38 min. This linear behavior indicates that the generation of reactive chemical species and their dissolution in the aqueous medium occur in a stable and continuous manner throughout the activation process.

This increase in σ highlights the influence of plasma treatment in modifying the electrochemical structure of the solution. The continuous generation of ions and reactive species dynamically alters the ionic composition of the medium, which not only reflects the efficiency of the process but also reinforces the importance of electrical conductivity as a key parameter for monitoring the chemical and electrochemical impact of plasma on the activated solution [18, 31].

Dissolved oxygen (DO) reflects the interaction between plasma and the aqueous medium, indicating the formation of ROS, such as free radicals, ozone (O_3), and peroxides. These species play an essential role in the antimicrobial activity of activated solutions, promoting the oxidation of biomolecules and destabilization of cell membranes, contributing to microorganism inactivation [32]. In Fig. 7e, a sharp drop in DO is observed in the first 4 min, from approximately 10 mg/L to 6 mg/L, due to the rapid consumption of dissolved oxygen for ROS generation. After this period, DO stabilizes at around 6 mg/L, suggesting a dynamic equilibrium between the consumption and generation of new chemical species. These changes impact properties such as pH and ORP, making DO a relevant indicator for monitoring the dynamics of chemical and biological transformations induced by plasma treatment.

Figure 7f shows the real-time mass of the DI water during plasma activation. The mass decreases monotonically from ~ 40 g at ignition to ~ 29 g at 38 min, reflecting evaporation driven by the plasma–liquid heat load. Small step-like fluctuations likely arise from transient jet instabilities or bubble release. Tracking mass in parallel with thermal and chemical metrics is therefore informative, as evaporation concentrates solutes and can bias apparent trends in TDS, electrical conductivity, and ORP.

To separate net RONS production from evaporative concentration, end-point values were normalized to the initial volume using the measured mass loss (40 g → 29 g; $V_{\text{final}}/V_{\text{initial}} = 0.725$). For any species,

$$C_{\text{norm}}(t) = C_{\text{meas}}(t) \times \frac{V_{\text{final}}(t)}{V_{\text{initial}}}. \quad (1)$$

Applied at 40 min, this yields $H_2O_2 \approx 19.0$ ppm (from 26.0 ppm), $NO_3^- \approx 17.4$ ppm (from 24.0 ppm), and $NO_2^- \approx 0.72$ ppm (from 0.99 ppm). Evaporation thus inflates raw concentrations by ~ 38% at the end point, but the temporal evolution and comparative conclusions remain unchanged.

3.4 Chemical Characterization of PAW

3.4.1 Colorimetric Assay

Colorimetric quantification of nitrite (NO_2^-), nitrate (NO_3^-), and hydrogen peroxide (H_2O_2) was performed using a Micro 20 Multiparameter Photometer (AKSO) with device-specific test strips for each analyte. The operational ranges were 0–60.0 ppm for NO_3^-, 0.01–1.80 ppm for NO_2^-, and 0.3–100 ppm for H_2O_2. Measurements were recorded at ten time points during plasma activation—0, 2.5, 5.0, 10.0, 15.0, 20.0, 25.0, 30.0, 35.0, and 40.0 min—so as to capture the time-resolved evolution of RONS under SWD activation in argon (Fig. 8). This approach revealed distinct temporal profiles for each species, reflecting the dynamic nature of plasma–liquid interactions in the SWD system and providing a quantitative baseline consistent with the spectroscopic signatures presented in the following subsection.

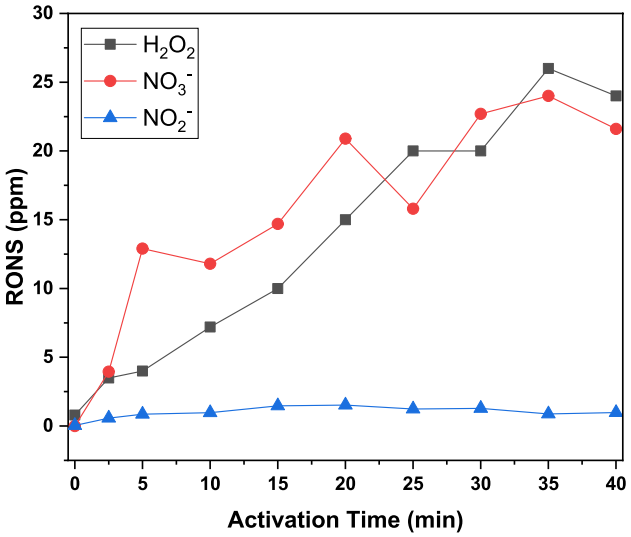

Fig. 8 Time evolution of reactive species in plasma-activated deionized water (PAW) during SWD-Ar treatment from 0–40 min: hydrogen peroxide (H_2O_2, squares), nitrate (NO_3^-, circles), and nitrite (NO_2^-, triangles). H_2O_2 and NO_3^- increase with activation time, reaching ~ 20–25 ppm by 30–40 min, while NO_2^- remains low ($\leq$ ~ 1 ppm) over the entire interval. Measurements were obtained at each time point for DI water treated for the indicated duration

Over the 40-min activation window, H_2O_2 rose in an almost linear fashion, reaching 26 ppm at 35 min and exhibiting a slight decline at 40 min, behavior consistent with continuous production followed by competing consumption/decomposition processes at longer times. NO_3^- likewise increased substantially, albeit with a nonlinear trajectory, showing fluctuations between 15 and 35 min and peaking at 24 ppm before a small decrease toward the end. In contrast, NO_2^- remained persistently low throughout the experiment, ending near 0.99 ppm, which suggests limited net formation and/or efficient oxidation to NO_3^- under the present plasma conditions. Given the method's low-end sensitivity and potential NO_2^-/H_2O_2 cross-interference, very low NO_2^- values should be viewed as approximate; this caveat does not affect the trends or conclusions. To isolate net production from evaporative concentration, 40-min end-point values were volume-normalized using the measured mass loss (40 g → 29 g; $V_{final}/V_{initial} = 0.725$), yielding $H_2O_2 \approx 19.0$ ppm, $NO_3^- \approx 17.4$ ppm, and $NO_2^- \approx 0.72$ ppm—adjustments that refine quantitative yields without changing the qualitative time evolution described above. This pattern supports limited net formation of NO_2^- and/or its rapid oxidation to NO_3^- under the present plasma conditions.

To contextualize these concentrations, a comparative analysis with representative plasma systems reported in the literature was conducted (Table 1), considering plasma type, working gas, power, treated volume, and activation time. These comparisons indicate that the SWD configuration favors a balanced RONS profile with prominent H_2O_2 accumulation while treating a moderate liquid volume without direct plasma–liquid contact, thereby maintaining chemical purity and reducing contamination risk. Such features are advantageous for biomedical and microbiological applications that require sterility and reproducibility.

Table 1 Comparison of plasma-activated water (PAW) production parameters and resulting concentrations of reactive oxygen and nitrogen species (RONS) in different plasma systems reported in the literature. The table includes plasma type, working gas, power input, liquid volume activated, activation time, and final concentrations of hydrogen peroxide (H_2O_2), nitrate (NO_3^-), and nitrite (NO_2^-). Data illustrate variations in RONS generation depending on plasma configuration, gas composition, and treatment conditions

	Plasma device	Working gas	Power	Volume (mL)	Activation Time (min)	H_2O_2	NO_3^-	NO_2^-
Our study	Surfatron (SWD)	Ar	70W	40	40	26.0	0.99	24.0
Volkov et al. (2021) [33]	CAPPJ	He	System powered by 8 kV, 6 kHz, 1 µs pulses	20	130	10.0	1.0	25.0
Sar et al. (2024) [34]	DBD jet	N_2	10-25W	6	10	0.26	2.3	4.5
Miranda et al. (2023)[29]	Coaxial DBD	Air	50W	25	10	3.0	5.00	500.0
Miranda et al. (2023) [29]	Coaxial DBD	Air	50W	50	10	2.11	3.06	366.2

To complement this chemical characterization, the energy efficiency of the SWD-based PAW production was also evaluated. For the argon-based plasma activation at 70 W over 40 min treating 40 mL of DI water, the total energy input was 46.67 Wh, corresponding to an energy per liter (EPL) of approximately 1.17 kWh L^{-1} (4.2 MJ L^{-1}). In comparison, coaxial DBD systems operating at 50 W for 10 min achieve significantly lower EPL values, such as 0.33 kWh L^{-1} when treating 25 mL and 0.17 kWh L^{-1} when treating 50 mL. Likewise, a DBD jet operating with N_2 at 10–25 W for 10 min applied to 6 mL of liquid results in EPL values ranging from 0.28 to 0.69 kWh L^{-1}. These differences underscore the influence of reactor design (e.g., contactless surface activation vs. direct submersion), gas composition, and mass transfer dynamics on energy performance. Although the SWD system requires a higher energy input per liter, it offers superior chemical purity and eliminates risks associated with electrode erosion and metal contamination. Moreover, the energy demand could be significantly reduced through straightforward optimizations, such as reducing the nozzle–liquid gap, incorporating O_2/N_2 admixtures, implementing bubbling or recirculation strategies, and adopting active cooling mechanisms to enhance RONS transfer and reduce evaporation losses.

3.4.2 UV–Vis Spectrophotometry

UV–Vis spectroscopy (190–270 nm) provided complementary, qualitative fingerprints of PAW composition (Fig. 9). As activation time increased, the overall absorbance rose and characteristic features assigned to H_2O_2, HNO_2, NO_3^-, NO_2^-, and O_3 became more pronounced, corroborating the colorimetric trends and indicating sustained formation of reactive species in the aqueous phase.

Figure 9a shows that UV absorbance across 190–270 nm increases with activation time, and that features attributable to H_2O_2, HNO_2, NO_3^-, NO_2^-, and O_3 become progressively more pronounced. These spectral changes corroborate the colorimetric trends in Fig. 8, indicating sustained formation of reactive oxygen and nitrogen species in the aqueous phase. Figure 9b quantifies this behavior via the integrated absorbance, which rises monotonically before its slope diminishes after ~ 20 min, signaling the onset of a dynamic balance between generation and consumption pathways. This late-time moderation is consistent with the plateau observed for H_2O_2 and NO_3^- (see §3.4.1) and aligns with thermal and evaporation constraints discussed elsewhere. Finally, colorimetric NO_2^- at sub-ppm levels is intrinsically uncertain under oxidant-rich conditions—an acknowledged limitation in Methods and Results—so very low NO_2^- values should be interpreted with appropriate caution.

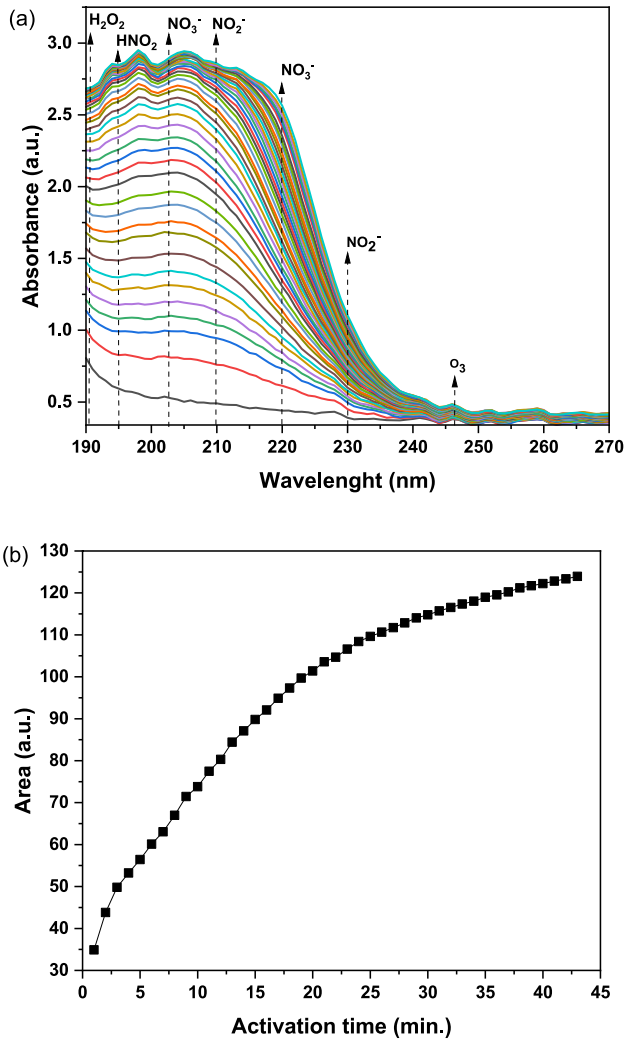

Fig. 9 (**a**) Time-resolved UV–Vis spectra (190–270 nm) of plasma-activated deionized water during SWD-Ar treatment from 0 to 40 min. Vertical dashed lines mark bands commonly attributed to oxidizing species in PAW: H_2O_2/HNO_2 (≈195–205 nm), the NO_3^- envelope (≈200–215 nm), a weak NO_2^- shoulder near ≈230 nm, and a residual feature near ≈260 nm (O_3). The 0-min DI water spectrum is shown for reference. (**b**) Integrated absorbance in the deep-UV region (190–230 nm) versus activation time, showing a monotonic increase and approaching a plateau after ~ 30–40 min, consistent with progressive accumulation of oxidized nitrogen species

The early-time increase followed by late-time moderation of H_2O_2 and NO_3^- is consistent with interfacial production pathways gradually being balanced by consumption and transport limits. In an argon jet that entrains ambient air, OH and HO_2 radicals formed near the gas–liquid interface promote H_2O_2 accumulation, while NO/NO_2 generated in the gas phase (and NO_2^- in the liquid) advance toward nitrate via aqueous oxidation. With prolonged activation, three effects temper further growth and yield the

spectral and colorimetric plateaus: (i) thermal/pH-assisted decomposition of H_2O_2, (ii) acid-driven consumption of nitrite along the pathway to nitrate, and (iii) mass-transfer constraints—including evaporation and limited gas–liquid exchange across the fixed nozzle–liquid gap. In future work, a reduced global kinetic model, constrained by our measured heat flux and evaporation-derived volume change, will quantify these competing channels and directly connect the evolving plasma state (temperatures/species from OES) to the time-resolved RONS yields reported here.

3.5 Microbiological assays

The comparative study of plasma-activated liquids was conducted using PAW to evaluate microbial inactivation efficacy under the same activation parameters. The microbiological assessment included three distinct microorganisms: the gram-positive bacterium *S. aureus* (ATCC 6538), the gram-negative bacterium *E. coli* (ATCC 10799), and the fungus *C. albicans* (SC 5314). Figure 10 summarizes the results obtained.

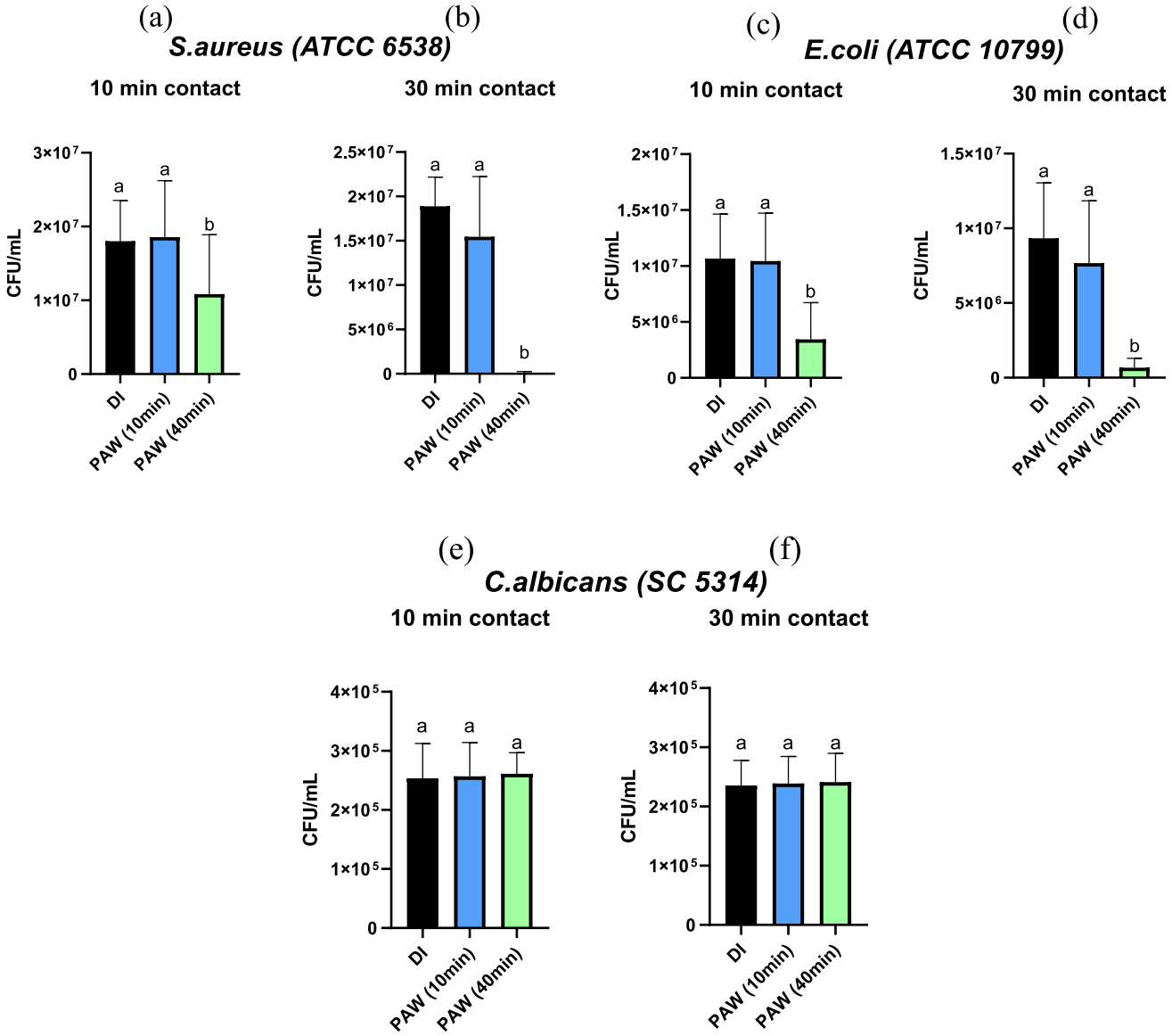

Fig. 10 Colony-forming unit counts (CFU mL^{-1}) for *Staphylococcus aureus* (ATCC 6538), *Escherichia coli* (ATCC 10799) and *Candida albicans* (SC 5314) after exposure to deionized water (DI, control) or plasma-activated water (PAW) generated for 10 or 40 min. Panels: (**a**–**b**) *S. aureus* after 10 and 30 min contact; (**c**–**d**) *E. coli* after 10 and 30 min; (**e**–**f**) *C. albicans* after 10 and 30 min. Bars show mean ± SD (n = 9 per group; three independent experiments × triplicate). Within each panel, different letters indicate significant differences among DI, PAW (10 min) and PAW (40 min) by one-way ANOVA followed by Tukey's post-hoc test (two-tailed, $\alpha = 0.05$)

The results indicate that contact time plays a crucial role in microbial inhibition. PAW demonstrated greater efficacy at prolonged contact times (30 min), as observed in Figs. 10b, 10d, and 10f. Additionally, the data suggest that bacteria were more susceptible to the treatment than the fungus *C. albicans*. Among the bacteria, the gram-positive *S. aureus* exhibited a more pronounced inhibition compared to the gram-negative *E. coli*, highlighting the influence of structural differences in the cell wall.

***Staphylococcus aureus* (ATCC 6538):** At 10 min of contact (Fig. 10a), no statistical differences were observed between DI and PAW treated for 10 min. However, PAW treated for 40 min showed a significant reduction in CFU/mL. At 30 min of contact (Fig. 10b), PAW treated for 40 min exhibited more pronounced inhibition, being statistically different from the other groups.

***Escherichia coli* (ATCC 10799):** For 10 min of contact (Fig. 10c), only PAW treated for 40 min resulted in a significant reduction, while the other groups showed no relevant differences. At 30 min of contact (Fig. 10d), PAW treated for 40 min exhibited a sharp decrease in CFU/mL, being statistically distinct from the other conditions.

***Candida albicans* (SC 5314):** At both 10 min (Fig. 10e) and 30 min of contact (Fig. 10f), no statistically significant differences were identified between DI and PAW treated for 10 and 40 min. CFU/mL values remained similar across all conditions.

These results reinforce the potential of PAW produced by SWD argon plasma as an effective tool for microbial inactivation, particularly against bacteria. The structure of cell walls appears to significantly influence microbial susceptibility, with *S. aureus* showing higher sensitivity due to its simpler gram-positive cell wall. On the other hand, the lack of a significant effect against *C. albicans* suggests that plasma inactivation mechanisms may be less effective against fungi, possibly due to differences in cellular composition or the inherent resistance of fungal cells.

3.6 Mechanisms of PAW Action in Microorganisms

The results show that treatment with PAW generated by activation with the SWD argon plasma is highly effective against the gram-positive bacterium *Staphylococcus aureus* and the gram-negative bacterium *E. coli*, particularly with longer activation and contact times. However, the limited efficacy against the fungus *Candida albicans* highlights the need to optimize the physicochemical parameters of PAW or combine approaches to enhance its action against more resistant microorganisms.

The antimicrobial efficacy of PAW is directly related to the physicochemical parameters analyzed previously. The significant reduction in CFU/mL for *S. aureus* and *E. coli* (Fig. 10a–d) can be attributed to the high concentration of RONS generated during plasma treatment. The acidification of PAW, with a decrease in pH, compromises the stability of bacterial cell membranes, interfering with homeostatic mechanisms. This process leads to protein denaturation, lipid peroxidation, and irreversible structural damage [21, 29]. Efficacy increases with longer activation times (40 min) and extended contact duration (30 min), amplifying the impact of reactive species.

Additionally, the increase in ORP reflects the high oxidative power of the solution, causing damage to essential biomolecules such as lipids, proteins, and nucleic acids [14, 31]. The rise in electrical conductivity (σ) and TDS also contributes to osmotic stress in bacteria, making cellular adaptation to the reactive environment more difficult. These mechanisms explain the higher vulnerability of *S. aureus*, while gram-negative bacteria such as *E. coli* exhibit greater initial resistance due to their outer cell wall acting as a barrier.

The differential action of reactive oxygen and nitrogen species (RONS) on cellular structures explains the varying susceptibilities of microorganisms to plasma-activated water (PAW). In gram-positive bacteria, such as *S. aureus*, RONS can readily penetrate the thick peptidoglycan cell wall and reach intracellular components, causing oxidative damage to proteins, lipids, and nucleic acids [21, 29]. This extensive intracellular damage leads to irreversible cellular stress and, ultimately, cell death (Fig. 11).

In contrast, gram-negative bacteria, such as *E. coli*, possess an outer membrane that serves as an additional protective barrier. As a result, RONS tend to accumulate primarily in the outer membrane and periplasmic space, with limited penetration into the cytoplasm. This restricted diffusion delays the antimicrobial effect, allowing *E. coli* to maintain cellular integrity for a longer period compared to gram-positive bacteria (Fig. 11) [21, 29].

On the other hand, the limited efficacy against *C. albicans* can be attributed to its unique structural characteristics. Unlike bacteria, fungi have a thick and highly complex cell wall composed of chitin, glycoproteins, and β-glucans [29]. This multi-layered structure acts as both a physical and chemical barrier, significantly hindering the penetration of RONS. Moreover, *C. albicans* possesses advanced antioxidant defense mechanisms, including enzymes like catalase and superoxide dismutase, which effectively neutralize a portion of the oxidative stress imposed by PAW, further enhancing fungal resilience (Fig. 11) [35–37].

These findings underscore that the efficacy of PAW depends not only on its physicochemical parameters but also on the specific structural and biochemical characteristics of the target microorganisms. The differences between bacterial and fungal cells, as well as the variations between gram-positive and gram-negative bacteria, highlight the importance of tailoring plasma-based antimicrobial strategies to effectively address more resistant microorganisms.

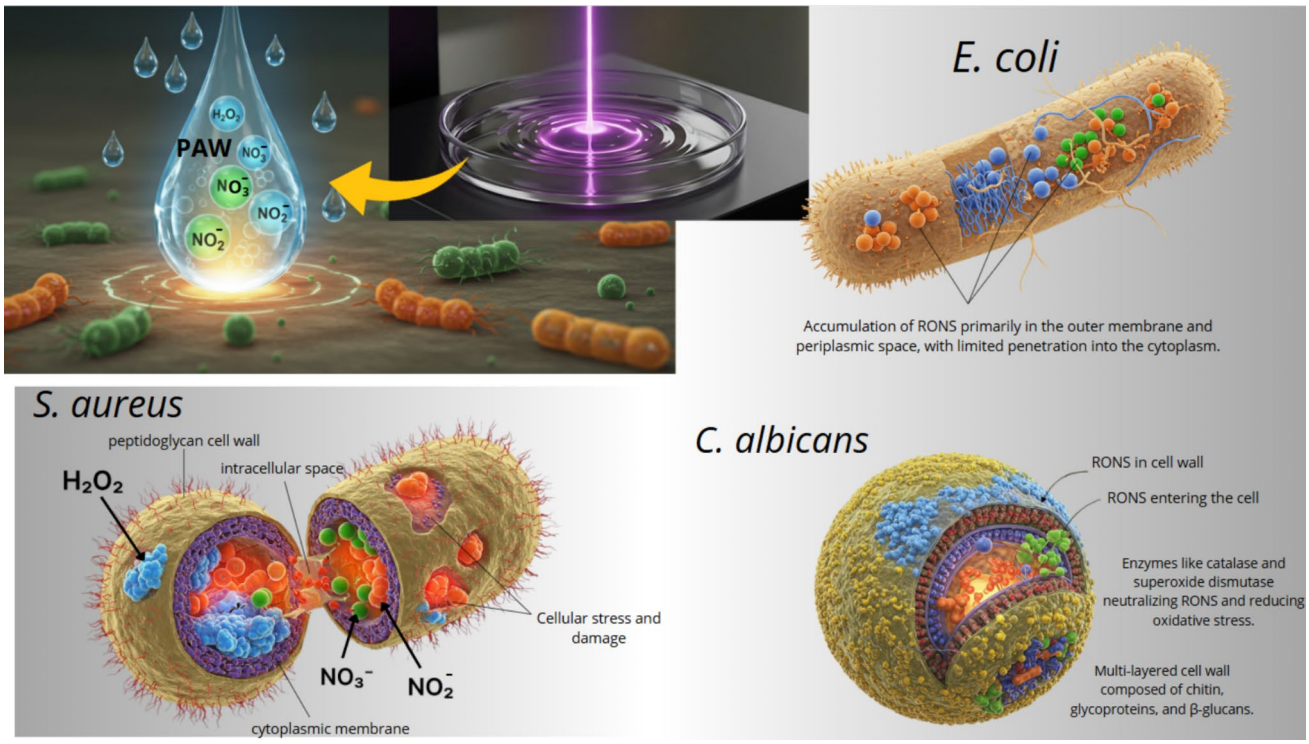

Fig. 11 Differential action of reactive oxygen and nitrogen species (RONS) on microbial cells exposed to plasma-activated water (PAW). The illustration highlights how the structural differences among microorganisms affect their susceptibility to RONS. In *S. aureus* (gram-positive), RONS penetrate the cell wall and reach intracellular components, causing extensive damage. In *E. coli* (gram-negative), RONS accumulate in the outer membrane and periplasmic space, delaying their antimicrobial effect. In *C. albicans* (fungus), the complex cell wall composed of chitin, glycoproteins, and β-glucans limits RONS penetration, while antioxidant enzymes further neutralize oxidative stress

4 Conclusion

Using an electrode-less SWD argon jet, we generated chemically clean PAW with reproducible, time-resolved physicochemical evolution—pH decreased to approximately 3.34; ORP increased to ~ 230 mV; electrical conductivity rose to ~ 180 µS/cm; TDS stabilized around 55 mg/L; and reactive species accumulated in measurable amounts (H_2O_2 between 10 and 25 mg/L, NO_3^- in the same range, and NO_2^- remaining below 1 mg/L) over a 40-min activation period. These results confirm that SWD activation modulates the coupled thermal and chemical dynamics of the plasma–liquid interface, producing stable and controllable PAW without direct bubbling or electrode contact, thus ensuring chemical purity and operational robustness.

The resulting PAW proved strongly bactericidal against *S. aureus* and *E. coli*, but not effective against *C. albicans*, highlighting the role of cell wall architecture and oxidative defense mechanisms in modulating organism-specific responses. This contrast also reinforces the importance of optimizing plasma conditions for broader antimicrobial spectrum. The antimicrobial action of PAW was driven by oxidative stress, combining acidification (which destabilizes microbial homeostasis), increased ORP (which enhances redox potential), and elevated conductivity and TDS (which cause osmotic imbalance and cellular damage).

Thermal measurements showed that the presence of water buffered the heat load, limiting excessive temperature rise during activation. Nonetheless, mild heating to ~ 40 °C under prolonged treatment could accelerate H_2O_2 degradation, indicating that future systems may benefit from active cooling or real-time temperature regulation. Simultaneously, volume reduction due to evaporation during longer exposures likely intensified RONS concentrations, contributing to stronger physicochemical effects but requiring careful balance between efficacy and stability.

We also quantified the energy-per-liter (≈1.17 kWh L^{-1}), showing that while the SWD configuration favors high chemical purity and contactless operation, it currently presents a higher energy cost compared to conventional DBD systems. However, this trade-off can be mitigated through minor gas admixtures (e.g., N_2/O_2), reduced nozzle-to-liquid distance, bubbling or recirculation strategies, and thermal management to improve both RONS generation and energy efficiency.

In summary, this work demonstrates that SWD-based PAW generation offers a clean, stable, and reproducible platform with strong bactericidal efficacy, particularly suited for applications where sterility and purity are critical. By elucidating the thermal, chemical, and biological aspects of the process and addressing key operational parameters, this study contributes to guiding future optimizations toward sustainable and targeted plasma-based antimicrobial solutions.

Acknowledgements The authors acknowledge financial support from The São Paulo State Research Foundation (FAPESP, grants 2019/05856-7, 2021/14181–3, 2022/13141-0, and 2022/10544-0).

Author contributions Author Contributions — Conceptualization, R.S.P., C.K.-I., and M.S.; Methodology, M.S., L.G., N.F.A.N., F.S.M., L.D.L., and V.K.F.T.; Investigation, M.S., L.G., F.S.M., L.D.L., and V.K.F.T.; Formal analysis, M.S. and F.S.M.; Resources, R.S.P., C.K.-I., and C.A.J.; Data curation, M.S., L.G., and L.D.L.; Visualization, M.S. and L.G.; Writing—original draft, M.S.; Writing—review & editing, M.S., F.S.M., N.F.A.N., C.A.J., C.K.-I., and R.S.P.; Supervision, R.S.P. and C.K.-I.; Project administration, R.S.P.; Funding acquisition, R.S.P. and C.K.-I. All authors reviewed and approved the final manuscript and agree to be accountable for all aspects of the work.

Data Availability All data supporting the findings of this study are included within the article and its supplementary materials.

Declarations

Competing interests The authors declare no competing interests.

References

1. A.G. da Sampaio, W. Chiappim, N.V.M. Milhan, B. Botan Neto, R. Pessoa, C.Y. Koga-Ito, Effect of the pH on the antibacterial potential and cytotoxicity of different plasma-activated liquids. Int. J. Mol. Sci. (2022). https://doi.org/10.3390/ijms232213893
2. N.V.M. Milhan, W. Chiappim, A. da G. Sampaio, M.R. da Cruz Vegian, R.S. Pessoa, C.Y. Koga-ito, Applications of plasma-activated water in dentistry: a review. Int. J. Mol. Sci. (2022). https://doi.org/10.3390/ijms23084131
3. D. Guo, H. Liu, L. Zhou, J. Xie, C. He, Plasma-activated water production and its application in agriculture. J. Sci. Food Agric. **101**, 4891–4899 (2021). https://doi.org/10.1002/jsfa.11258
4. Q.-Y. Han, X. Wen, J.-Y. Gao, C.-S. Zhong, Y.-Y. Ni, Application of plasma-activated water in the food industry: a review of recent research developments. Food Chem. **405**, 134797 (2023). https://doi.org/10.1016/j.foodchem.2022.134797
5. S. Kooshki, P. Pareek, R. Mentheour, M. Janda, Z. Machala, Efficient treatment of bio-contaminated wastewater using plasma technology for its reuse in sustainable agriculture. Environ. Technol. Innov. (2023). https://doi.org/10.1016/j.eti.2023.103287
6. Q. Tang, Z. Hu, X. Cui, Z. Tao, J. Tang, A simple and stable atmospheric pressure electrodeless water vapor microwave plasma torch. Appl. Sci. (2022). https://doi.org/10.3390/app12136813
7. E. Benova, P. Marinova, M. Atanasova, T. Petrova, Surface-wave-sustained argon plasma kinetics from intermediate to atmospheric pressure. J. Phys. D Appl. Phys. (2018). https://doi.org/10.1088/1361-6463/aae34d
8. M.A. Ridenti, N. Spyrou, J. Amorim, The crucial role of molecular ions in the radial contraction of argon microwave-sustained plasma jets at atmospheric pressure. Chem. Phys. Lett. **595–596**, 83–86 (2014). https://doi.org/10.1016/j.cplett.2014.01.050
9. K. Oehmigen, M. Hähnel, R. Brandenburg, C. Wilke, K.D. Weltmann, T. Von Woedtke, The role of acidification for antimicrobial activity of atmospheric pressure plasma in liquids. Plasma Processes Polym. **7**, 250–257 (2010). https://doi.org/10.1002/ppap.200900077
10. P. Bruggeman, C. Leys, Non-thermal plasmas in and in contact with liquids. J. Phys. D Appl. Phys. (2009). https://doi.org/10.1088/0022-3727/42/5/053001
11. N.F. Azevedo Neto, F.S. Miranda, P.W.P. Moreira Junior, M.P. Gomes, C.A. Junior, C.Y. Koga-Ito, R.S. Pessoa, Physical and chemical characteristics of plasma-activated water generated by hybrid dielectric barrier discharge and gliding arc discharge. J. Phys. D Appl. Phys. (2024). https://doi.org/10.1088/1361-6463/ad61f4
12. M.C. García, M. Mora, D. Esquivel, J.E. Foster, A. Rodero, C. Jiménez-Sanchidrián, F.J. Romero-Salguero, Microwave atmospheric pressure plasma jets for wastewater treatment: degradation of methylene blue as a model dye. Chemosphere **180**, 239–246 (2017). https://doi.org/10.1016/j.chemosphere.2017.03.126
13. A.C.O.C. Doria, F.R. Figueira, J.S.B. Lima, H.S. Maciel, S. Khouri, R.S. Pessoa, Surfatron-produced atmospheric-pressure plasma jet applied to *Candida* biofilms. Plasma Med. **4**, 345–355 (2019). https://doi.org/10.1615/PlasmaMed.2019028856
14. R. Ma, G. Wang, Y. Tian, K. Wang, J. Zhang, J. Fang, Non-thermal plasma-activated water inactivation of food-borne pathogen on fresh produce. J. Hazard. Mater. **300**, 643–651 (2015). https://doi.org/10.1016/j.jhazmat.2015.07.061
15. B. Ghimire, E.J. Szili, B.L. Patenall, P. Lamichhane, N. Gaur, A.J. Robson, D. Trivedi, N.T. Thet, A.T.A. Jenkins, E.H. Choi, R.D. Short, Enhancement of hydrogen peroxide production from an atmospheric pressure argon plasma jet and implications to the antibacterial activity of plasma activated water. Plasma Sources Sci. Technol. (2021). https://doi.org/10.1088/1361-6595/abe0c9
16. E. Benova, P. Marinova, R. Tafradjiiska-hadjiolova, Z. Sabit, D. Bakalov, N. Valchev, L. Traikov, T. Hikov, I. Tsonev, T. Bogdanov, Characteristics of 2.45 GHz Surface-Wave-Sustained Argon Discharge for Bio-Medical Applications. Appl. Sci. (Switzerland). **12** (2022). https://doi.org/10.3390/app12030969
17. Q. Zhang, R. Ma, Y. Tian, B. Su, K. Wang, S. Yu, J. Zhang, J. Fang, Sterilization efficiency of a novel electrochemical disinfectant against *Staphylococcus aureus*. Environ. Sci. Technol. **50**, 3184–3192 (2016). https://doi.org/10.1021/acs.est.5b05108
18. K.S. Wong, N.S.L. Chew, M. Low, M.K. Tan, Plasma-activated water: physicochemical properties, generation techniques, and applications. Processes (2023). https://doi.org/10.3390/pr11072213
19. P. Bourke, D. Ziuzina, L. Han, P.J. Cullen, B.F. Gilmore, Microbiological interactions with cold plasma. J. Appl. Microbiol. **123**, 308–324 (2017). https://doi.org/10.1111/jam.13429
20. Q.-Y. Han, Z.-Y. He, C.-S. Zhong, X. Wen, Y.-Y. Ni, The optimization of plasma activated water (PAW) generation and the inactivation mechanism of PAW on *Escherichia coli*. J. Food Process. Preserv. **46**, e17120 (2022). https://doi.org/10.1111/jfpp.17120
21. Y.M. Zhao, S. Ojha, C.M. Burgess, D.W. Sun, B.K. Tiwari, Inactivation efficacy of plasma-activated water: influence of plasma treatment time, exposure time and bacterial species. Int. J. Food Sci. Technol. **56**, 721–732 (2021). https://doi.org/10.1111/ijfs.14708
22. G. Kamgang-Youbi, J.M. Herry, T. Meylheuc, J.L. Brisset, M.N. Bellon-Fontaine, A. Doubla, M. Naïtali, Microbial inactivation using plasma-activated water obtained by gliding electric discharges. Lett. Appl. Microbiol. **48**, 13–18 (2009). https://doi.org/10.1111/j.1472-765X.2008.02476.x

23. F.S. Miranda, V.K.F. Tavares, D.M. Silva, N.V.M. Milhan, N.F.A. Neto, M.P. Gomes, R.S. Pessoa, C.Y. Koga-Ito, Influence of gas type on reactive species formation, antimicrobial activity, and cytotoxicity of plasma-activated water produced in a coaxial DBD reactor. Plasma Chem. Plasma Process. (2024). https://doi.org/10.1007/s11090-024-10475-7
24. H. Xu, C. Liu, Q. Huang, Enhance the inactivation of fungi by the sequential use of cold atmospheric plasma and plasma-activated water: synergistic effect and mechanism study. Chem. Eng. J. (2023). https://doi.org/10.1016/j.cej.2022.139596
25. X. Lu, G.V. Naidis, M. Laroussi, S. Reuter, D.B. Graves, K. Ostrikov, Reactive species in non-equilibrium atmospheric-pressure plasmas: generation, transport, and biological effects. Phys. Rep. **630**, 1–84 (2016). https://doi.org/10.1016/j.physrep.2016.03.003
26. W. Chiappim, AdaG. Sampaio, F. Miranda, M. Fraga, G. Petraconi, A. da Silva Sobrinho, K. Kostov, C. Koga-Ito, R. Pessoa, Antimicrobial effect of plasma-activated tap water on *Staphylococcus aureus*, *Escherichia coli*, and *Candida albicans*. Water (2021). https://doi.org/10.3390/w13111480
27. A.A. Miles, S.S. Misra, J.O. Irwin, The estimation of the bactericidal power of the blood. J. Hyg. (Lond.). **38**, 732–749 (1938). https://doi.org/10.1017/s002217240001158x
28. N. Bolouki, W.H. Kuan, Y.Y. Huang, J.H. Hsieh, Characterizations of a plasma-water system generated by repetitive microsecond pulsed discharge with air, nitrogen, oxygen, and argon gases species. Appl. Sci. (2021). https://doi.org/10.3390/app11136158
29. F.S. Miranda, V.K.F. Tavares, M.P. Gomes, N.F.A. Neto, W. Chiappim, G. Petraconi, R.S. Pessoa, C.Y. Koga-Ito, Physicochemical characteristics and antimicrobial efficacy of plasma-activated water produced by an air-operated coaxial dielectric barrier discharge plasma. Water (2023). https://doi.org/10.3390/w15234045
30. N. Alemayehu, Assessment of Livestock Environment Interactions under crop-livestock production systems of Central Ethiopian Highlands. (2013). https://doi.org/10.13140/RG.2.1.4124.2482.
31. R. Thirumdas, A. Kothakota, U. Annapure, K. Siliveru, R. Blundell, R. Gatt, V.P. Valdramidis, Plasma activated water (PAW): chemistry, physico-chemical properties, applications in food and agriculture. Trends Food Sci. Technol. **77**, 21–31 (2018). https://doi.org/10.1016/j.tifs.2018.05.007
32. B. Nowruzi, H. Beiranvand, F.M. Aghdam, R. Barandak, The effect of plasma activated water on antimicrobial activity of silver nanoparticles biosynthesized by cyanobacterium *Alborzia kermanshahica*. BMC Biotechnol. **24**, 75 (2024). https://doi.org/10.1186/s12896-024-00905-x
33. A.G. Volkov, A. Bookal, J.S. Hairston, J. Roberts, G. Taengwa, D. Patel, Mechanisms of multielectron reactions at the plasma/water interface: interfacial catalysis, RONS, nitrogen fixation, and plasma activated water. Electrochim. Acta (2021). https://doi.org/10.1016/j.electacta.2021.138441
34. S. Sar, S. Mathews, M. Shneider, Sohail, H. Zaidi, S.H. Zaidi, RONS Concentration Measurements in Plasma-Activated Water. (2024). https://www.begellhouse.com. Accessed 02/06/2024
35. J. Wang, R. Han, X. Liao, T. Ding, Application of plasma-activated water (PAW) for mitigating methicillin-resistant *Staphylococcus aureus* (MRSA) on cooked chicken surface. LWT **137**, 110465 (2021). https://doi.org/10.1016/j.lwt.2020.110465
36. M. Ibañez Olvera, J. L. Tapia Fabela, J. A. Salazar Torres, R. Z. García Lozano, Simulación de arco eléctrico deslizante en configuración de tres electrodos usando software libre. Programación Matemática y Software. 8(3), 9–16 (2016). https://doi.org/10.30973/progmat/2016.8.3/2
37. Y. Kusano, S.V. Singh, A. Bardenshtein, N. Krebs, N. Rozlosnik, Plasma surface modification of glass-fibre-reinforced polyester enhanced by ultrasonic irradiation. J. Adhes. Sci. Technol. 1831–1839 (2010). https://doi.org/10.1163/016942410X507605
38. D. Taheri, K. Hajisharifi, E. Heydari, F.K. MirzaHosseini, H. Mehdian, E. Robert, Realtime RONS monitoring of cold plasma-activated aqueous media based on time-resolved phosphorescence spectroscopy. Sci. Rep. **14**, 22403 (2024). https://doi.org/10.1038/s41598-024-73585-4